Propagation and circulating modes of the reciprocal non-Hermitian skin effect

Issei Takeda [1,2], Taiki Yoda [1], Yuto Moritake [1], Kenta Takata [2,3] and Masaya Notomi [1,2,3]

[1]*Department of Physics, Institute of Science Tokyo, 2-12-1 Ookayama, Meguro-ku, Tokyo 152-8550, Japan*

[2]*NTT Basic Research Laboratories, NTT, Inc., 3-1 Morinosato Wakamiya, Atsugi-shi, Kanagawa 243-0198, Japan*

[3]*Nanophotonics Center, NTT, Inc., 3-1 Morinosato Wakamiya, Atsugi-shi, Kanagawa 243-0198, Japan*

(Received 5 June 2025; accepted 6 October 2025; published 3 November 2025)

The non-Hermitian skin effect (NHSE) is a novel localization phenomenon, in which all bulk states in a non-Hermitian system under certain conditions are localized at the edge of the system. Conventionally, most studies of NHSE have dealt with discrete lattice systems with nonreciprocal couplings. However, in recent years, NHSE in a reciprocal two-dimensional continuous medium, such as photonic crystal systems, has also been reported. In particular, we have previously shown that NHSE also occurs in two-dimensional uniform media. In such two-dimensional systems, skin modes propagate in a direction perpendicular to the localization direction and, in particular, they have the property of propagating in only one direction. In this paper, we show numerically an intriguing scattering phenomenon: when a scatterer is placed in the path of a skin mode, the scattering causes the skin mode to hop between opposing edges. In addition, we propose a unique method of generating circulating modes with orbital angular momentum (OAM) using this scattering phenomenon. Our work paves the way for more applications of NHSE as microsized optical devices manipulating or generating OAM.

DOI: 10.1103/gqlb-qxkl

I. INTRODUCTION

Non-Hermitian systems with gain or loss have attracted much attention in recent years because of the appearance of novel phenomena that have not been realized in Hermitian systems. Optical systems are a suitable platform for exploring non-Hermitian physics because non-Hermiticity can be easily introduced by gains and losses caused by materials. In particular, studies in optical systems with parity-time ($\mathcal{PT}$) symmetry [1] have been intensive, and many peculiar phenomena have been reported, such as asymmetric light propagation [2–4], unidirectional invisibility [5–7], and fast-light states [8].

One of the phenomena unique to non-Hermitian systems is the non-Hermitian skin effect (NHSE) [9,10], a phenomenon in which all bulk eigenstates are localized at the edge of the system under open boundary conditions in certain non-Hermitian systems. In Hermitian systems and non-Hermitian systems without NHSE, bulk states extended throughout the system usually form a continuous energy spectrum. On the other hand, in non-Hermitian systems where NHSE occurs, localized states at the edges of the system form a continuous spectrum. Many of the early studies of NHSE dealt with one-dimensional discrete lattice models with asymmetric coupling, as shown in Fig. 1(a), and experiments have subsequently reported on many systems based on these models, including optical systems [11,12], mechanical systems [13–15], electrical circuits [16,17], acoustic systems [18], and ultracold atoms [19].

However, in recent years, NHSE has also been reported in continuous systems such as photonic crystals with anisotropic structures [20–22] or anisotropic media [23,24], and anisotropic uniform media [25], which are described by differential equations such as Maxwell's equations. In particular, propagation has not been considered in the conventional NHSE studies. However, in a continuous medium, skin modes become two-dimensional propagating states because they have a wave vector component in the direction perpendicular to the localization direction [Fig. 1(b)]. Previous studies of NHSE in optical systems have shown that in infinitely long stripe systems, i.e., with periodic boundary conditions in one direction, the localized position of skin modes depends on the propagation direction, and when the propagation direction is reversed, the localized position also reverses [20,23,25]. Therefore, skin modes propagate in only one direction at one edge. However, there are no reports on the properties of the propagating skin modes, such as transmission or reflection. Moreover, there have been some studies of NHSE in finite systems [21,22,24], but none of them have focused on unidirectional propagation.

In this work, we numerically investigate properties of skin mode propagation in finite two-dimensional systems. First, we simulate the skin mode in the system with the mirror-time ($\mathcal{MT}$) symmetric medium [25,26], an anisotropic medium with balanced gain and loss and a scatterer in the path of the skin mode. Then we found an intriguing scattering phenomenon in which the backscattering of the skin mode is suppressed, instead hopping to the opposite edge. Also, the excited skin mode and the hopped skin mode propagated in opposite directions, and in total, we confirmed that it was a rotationlike mode. Furthermore, we have applied the scattering phenomenon of skin modes to consider closed systems surrounded by reflective boundaries. Initially, we considered a square structure, and skin modes appeared at the top, bottom, left, and right edges. Skin modes on the left and right edges propagated clockwise, while skin modes on the top and bottom edges propagated counterclockwise, and they were balanced. However, by considering the rectangular structure,

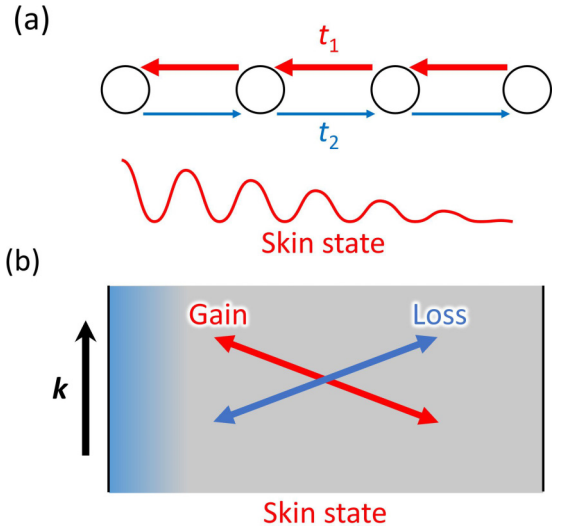

FIG. 1. (a) Skin state in one-dimensional crystal. (b) Skin state in two-dimensional continuous medium.

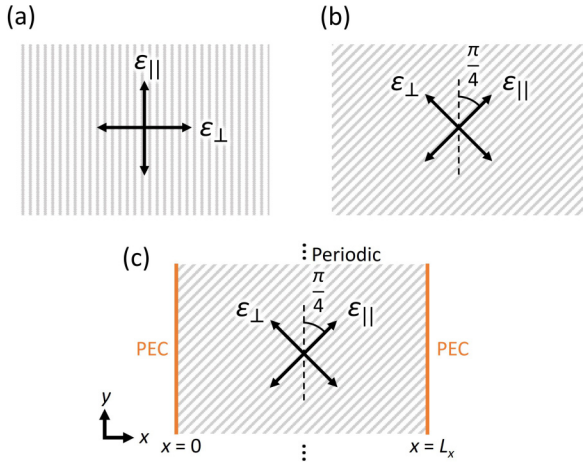

FIG. 2. [(a),(b)] Schematics of anisotropic uniform medium and 45° tilted anisotropic uniform medium, respectively. (c) Infinitely long stripe structure with 45° tilted medium.

one of the rotations was strongly manifested, and we succeeded in generating the optical orbital angular momentum (OAM) [27] by a method using NHSE. We also discuss the application of the geometry dependence of NHSE [21,22,28,29] to improve the efficiency of the OAM.

Finally, we confirmed that OAM generation by NHSE was feasible, even when using loss-biased media, which are easy to realize.

II. NHSE IN UNIFORM MEDIA

A. Analytical solution of NHSE in uniform media

Conventional studies of optical NHSE have dealt with systems with a periodically modulated dielectric constant, such as photonic crystals. On the other hand, we have recently shown that NHSE can be realized even in media with a uniform dielectric permittivity [25]. The realization of NHSE requires the non-Hermiticity and the anisotropy of the dielectric tensor, and in a uniform medium, it is easy to control them. In addition, the analytical solution of NHSE can be derived. Thus, in this work, we deal with the propagation of NHSE in a reciprocal uniform medium.

First, the dielectric tensor of a medium with non-Hermitian anisotropy, as shown in Fig. 2(a), is given by

$$\begin{pmatrix} \varepsilon_{\perp} & 0 & 0 \\ 0 & \varepsilon_{\parallel} & 0 \\ 0 & 0 & \varepsilon_z \end{pmatrix}, \tag{1}$$

where $\varepsilon_{\parallel}$ and $\varepsilon_{\perp}$ have nonzero imaginary parts. Here we consider a medium with anisotropy axes tilted 45° as shown in Fig. 2(b). In this case, the dielectric tensor is given by

$$\begin{pmatrix} \varepsilon_{xx} & \varepsilon_{xy} & 0 \\ \varepsilon_{yx} & \varepsilon_{yy} & 0 \\ 0 & 0 & \varepsilon_{zz} \end{pmatrix} = \begin{pmatrix} (\varepsilon_{\parallel}+\varepsilon_{\perp})/2 & (\varepsilon_{\parallel}-\varepsilon_{\perp})/2 & 0 \\ (\varepsilon_{\parallel}-\varepsilon_{\perp})/2 & (\varepsilon_{\parallel}+\varepsilon_{\perp})/2 & 0 \\ 0 & 0 & \varepsilon_z \end{pmatrix}, \tag{2}$$

when we consider the transverse electric mode $H_z(x,y,t) = e^{i(\omega t - k_y y)} H_z(x)$ traveling in the y direction in a system with finite width L_x with periodic boundary conditions (PBCs) imposed in the y direction and perfect electric conductors (PECs) boundary condition in the x direction, as shown in Fig. 2(c). In this system, the eigenstates can be obtained analytically [25]:

$$\left(\frac{\omega}{c}\right)^2 = \eta_{yy}\left(\frac{\pi n}{L_x}\right)^2 + (\eta_{xx} - q^2\eta_{yy})k_y^2; n = 1, 2, \ldots, \tag{3}$$

$$E_y(x) = e^{iqk_y x} \sin\left(\frac{\pi n}{L_x}x\right), \tag{4}$$

$$H_z(x) = \frac{1}{2} i e^{iqk_y x}\left[\left(\frac{1}{Z_{x+}} - \frac{1}{Z_{x-}}\right)\cos\left(\frac{\pi n}{L_x}x\right) - i\left(\frac{1}{Z_{x+}} + \frac{1}{Z_{x-}}\right)\sin\left(\frac{\pi n}{L_x}x\right)\right], \tag{5}$$

$$E_x(x) = -\frac{1}{2} i e^{iqk_y x}\left[\left(\frac{Z_{y+}}{Z_{x+}} - \frac{Z_{y-}}{Z_{x-}}\right)\cos\left(\frac{\pi n}{L_x}x\right) - i\left(\frac{Z_{y+}}{Z_{x+}} + \frac{Z_{y-}}{Z_{x-}}\right)\sin\left(\frac{\pi n}{L_x}x\right)\right], \tag{6}$$

where c is the speed of light in vacuum; η_{ij} is the component of the inverse tensor of the dielectric tensor; and $q, k_{\pm}, Z_{x\pm}, Z_{y\pm}$ are defined as follows:

$$q = \frac{\varepsilon_{xy} + \varepsilon_{yx}}{2\varepsilon_{xx}}, \tag{7}$$

$$k_{\pm} = \pm\frac{\pi n}{L_x} - qk_y, \tag{8}$$

$$Z_{x\pm} = \frac{1}{\omega\varepsilon_0}(-k_y\eta_{yx} + k_{\pm}\eta_{yy}), \tag{9}$$

$$Z_{y\pm} = \frac{1}{\omega\varepsilon_0}(k_y\eta_{xx} - k_{\pm}\eta_{xy}), \tag{10}$$

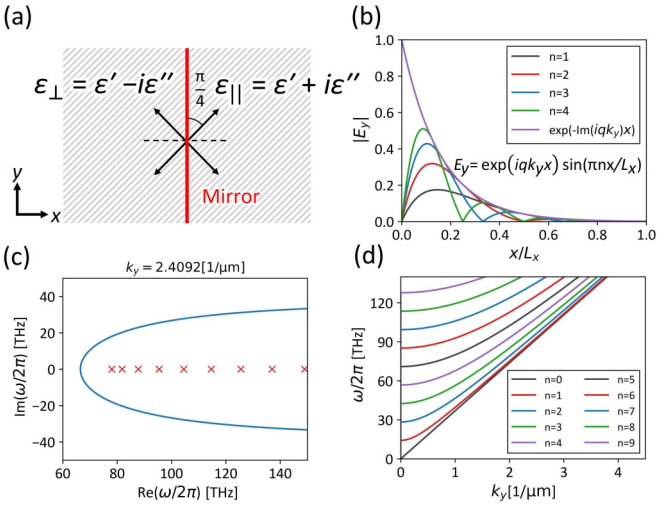

FIG. 3. (a) $\mathcal{MT}$ symmetric medium. (b) Eigenfrequency spectra under periodic boundary condition and open boundary condition. (c) Relationship between k_y and eigenfrequencies in the system shown in (a). (d) Eigenmodes in the infinitely long stripe system with $\mathcal{MT}$ symmetric medium.

where ε_0 is the dielectric permittivity in vacuum. From Eqs. (4)–(6), the state is localized when $\mathrm{Im}(q) \neq 0$ and $k_y \neq 0$. When the medium is not tilted, $q = 0$ and no localization occurs, but when tilted, if $\varepsilon_\perp$ and $\varepsilon_\parallel$ are appropriately chosen, a nonzero imaginary part of q can be realized and skin modes appear.

Here, from Eqs. (4)–(6), it can be seen that when the direction of skin mode propagation is reversed, i.e., the sign of k_y is reversed, the localization position is also reversed. Thus the skin mode propagates in only one direction at one edge. Similar to the unidirectional propagation seen in topological edge modes [30–32], backscattering may be suppressed also in the case of propagating skin modes.

B. $\mathcal{MT}$ symmetric media

We have simulated the propagation of skin modes with $\mathcal{MT}$ symmetric media [25,26]. Here, $\mathcal{MT}$ symmetry is the symmetry about mirror and time reversal. The mirror plane is a plane perpendicular to the x or y direction. The time reversal corresponds to a complex conjugate operation of dielectric constants. In non-Hermitian systems, $\mathcal{PT}$ symmetry is often discussed. $\mathcal{PT}$ and $\mathcal{MT}$ symmetry coincide in one-dimensional systems, but in two-dimensional systems, the operation by $\mathcal{P}$ is $(x, y) \mapsto (-x, -y)$, while the operation by $\mathcal{M}$ is $(x, y) \mapsto (-x, y)$ or $(x, y) \mapsto (x, -y)$, and they are different.

As shown in Fig. 3(a), $\mathcal{MT}$ symmetry is satisfied when it holds that $\varepsilon_\parallel = \varepsilon_\perp^*$. In $\mathcal{MT}$ symmetric media, q is a pure imaginary number. Thus, when $\mathrm{Re}(k_y) \neq 0$, eigenstates [Eqs. (4)–(6)] become localized states [Fig. 3(b)]. In a periodic structure like the photonic crystal system, the eigenfrequencies of skin modes are distributed in the closed loop of eigenfrequencies under the PBC on the complex frequency plane. On the other hand, in a uniform medium, the eigenfrequencies under the PBC form an open arc [25], and the eigenfrequencies of the skin modes are distributed inside the open arc. In particular, in an $\mathcal{MT}$ symmetric uniform medium, the open arc is symmetric to the real axis of the complex frequency plane, and the eigenfrequencies of the skin mode appear on the real axis inside the open arc [Fig. 3(c)]. In this case, from Eq. (3), k_y is also a real number. Here, the relationship between k_y and $\omega/2\pi$ is shown in Fig. 3(d). This property, where k_y and ω are both real numbers, allows for skin modes that are not amplified or attenuated in space or time, which is ideal for exploring propagation.

Here anisotropy as shown in Fig. 2 can be approximately realized by considering the effective medium model for a subwavelength multilayer metamaterial consisting of two different media, and obtaining $\varepsilon_\parallel$ and $\varepsilon_\perp$ as the dielectric constants in the direction parallel and perpendicular to the multilayer, respectively. In particular, the realization of an $\mathcal{MT}$ symmetric medium requires both a loss and a gain medium (see Appendix). In this work, we mainly use an $\mathcal{MT}$ symmetric medium ($\varepsilon_\parallel = \varepsilon_\perp^* = 1.673 + 0.965\,93i$), which is obtained from a loss medium and a gain medium with dielectric constants $\varepsilon_1 = 0.707\,11 - 0.707\,11i$ and $\varepsilon_2 = 2.639 + 2.639i$, respectively. In this case, components of the dielectric tensor are $\varepsilon_{xx} = \varepsilon_{yy} = 1.673$ and $\varepsilon_{xy} = \varepsilon_{yx} = 0.965\,93i$.

III. PROPAGATION OF SKIN MODES

A. Model for numerical calculation

A schematic of the structure is shown in Fig. 4(a). We consider the $\mathcal{MT}$ symmetric medium described above of finite width $L_x \sim 7.07$ μm (see Appendix A for how we determined the size of the structure) sandwiched between PECs in the x direction. Then we calculate by the finite element method by using COMSOL MULTIPHYSICS. We have also placed a square defect (length of one side d) at the left edge, and a perfectly matched layer (PML) [33] at the top and bottom to suppress reflections. We excite the propagating skin mode with a finite k_y value at port 1 where we set the light field profile for the $n = 1$ skin mode localized at the left edge determined by Eqs. (4)–(6). In addition to port 1, ports 2–4 are also placed for the detection of transmissions or reflections, and the scattering parameters (S_{11}, S_{21}, S_{31}, and S_{41}) are calculated for each port. Here, ports 1 and 2 detect a left-localized mode that propagates in the $-y$ and $+y$ directions, respectively. Also, ports 3 and 4 detect a right-localized mode that propagates in the $+y$ and $-y$ directions, respectively. The characteristics of the localization mode detected at each detection port are shown in Fig. 4(a).

B. Nature of unidirectional propagation

First, the simulation result excited at 90 THz for the no defect case ($d = 0$ μm) is shown in Fig. 4(b). Here, $k_y = 2.4092$ 1/μm from Eq. (3). In this case, skin modes without amplification or attenuation propagating in the $+y$ direction appeared. This skin mode should only be allowed to exist in the left edge and propagate in the $+y$ direction due to the propagation direction dependence of the localization position.

Next, Figs. 4(c)–4(e) show the calculated H_z distributions in a structure with a defect in the path of the skin mode

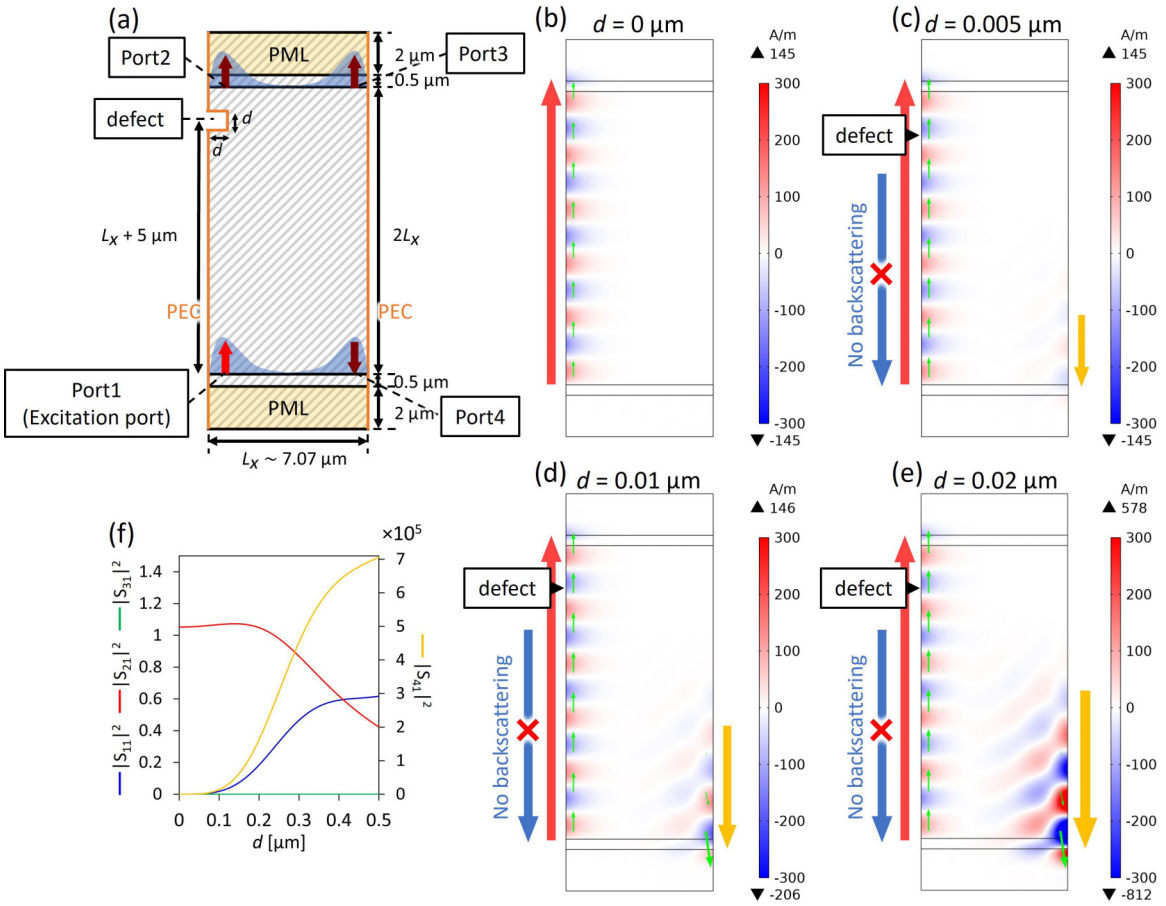

FIG. 4. (a) Schematic of the structure of the simulation. [(b)–(e)] Calculated H_z distribution for the length d of one side of the defect for $d = 0$ μm (i.e., no defect), $d = 0.005$ μm, $d = 0.01$ μm, and $d = 0.02$ μm, respectively. Green arrows show time-averaged Poynting vectors. Note that the Poynting vectors of the right edge are normalized to be as large as those of the left edge. (f) Relationship between transmittance, reflectance, and defect edge length d.

under the same excitation condition. Figure 4(c) shows that the left-localized skin mode is excited and looks almost the same as in Fig. 4(b). As expected there is no indication of the back reflection at the left edge (port 1). However, there is a finite intensity in the lower part of the right edge (port 4). This is due to interedge scattering caused by the introduction of the defect. Here, what is interesting is that corresponding to the fact that left-localized modes are not allowed to propagate in the $-y$ direction as eigenmodes in an infinitely long stripe system, reflections propagating on the left edge do not appear, and instead, interedge scattering at the defect induces $-y$ directional propagating modes on the right edge. As the size of the defect increases as shown in Figs. 4(d) and 4(e), it can be seen that the intensity of the skin mode on the right edge due to interedge scattering increases.

The calculated transmittances ($|S_{21}|^2$ and $|S_{31}|^2$) and reflectances ($|S_{11}|^2$ and $|S_{41}|^2$) of the skin mode are shown in Fig. 4(f). First, $|S_{31}|^2$ was always zero regardless of the defect size d, which indicates that no skin mode propagating in the $+y$ direction appears on the right edge. Next, the change of $|S_{21}|^2$ is small when d is small, and it begins to decrease when d is about 7% of the wavelength of the skin mode. In comparison, the change in $|S_{41}|^2$ was sensitive to the change in d, and the change in $|S_{41}|^2$ increased significantly when the defect size d was increased. This is thought to be because the right-localized skin mode is amplified by interedge scattering due to the right diagonal gain in the $\mathcal{MT}$ symmetric medium. Also, in Figs. 4(c)–4(e), no reflections of skin modes due to defect were observed on the left edge, and in Fig. 4(f), $|S_{11}|^2$ is indeed zero in $d = 0.005$ μm, 0.01 μm, and 0.02 μm. However, as d increases, $|S_{11}|^2$ also increases, which is thought to be due to the fact that some of the scattered waves are counted at port 1 as the right-localized skin mode is amplified due to interedge scattering. When we performed the same calculations in the 50–100 THz frequency range, we confirmed similar characteristics of transmittance and reflectance: $|S_{31}|^2$ is always zero, $|S_{21}|^2$ begins to decrease when d is around 6%–8%, $|S_{41}|^2$ increases significantly with d, and $|S_{11}|^2$ is zero when d is small and increases as $|S_{41}|^2$ increases.

Summarizing this section, we have described the results of our analysis of the unidirectional propagation of the skin mode and the properties of its scattering. In particular, we have shown that the scattering of the skin mode is peculiar, and that backscattering does not occur, but instead couples to the opposite edge. Furthermore, the overall skin mode progression was rotationlike. This result suggests a method for generating optical orbital angular momentum (OAM).

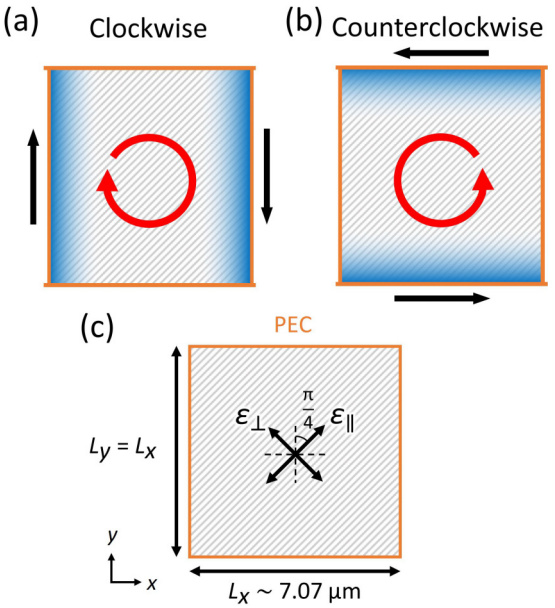

FIG. 5. [(a),(b)] show the modes that are expected to appear in the structure surrounded by the reflective boundaries. (a) Clockwise skin mode, localized on the left and right edges. (b) Counterclockwise skin mode, localized at the top and bottom edges. (c) The structure of the $\mathcal{MT}$ symmetric medium surrounded by PECs on the top, bottom, left, and right edges, used in the calculation.

IV. CIRCULATING SKIN MODES IN $\mathcal{MT}$ SYMMETRIC CASE

A. Numerical results for closed square structures

Inspired by the interedge scattering of skin modes described in the previous section, we consider a system with reflective bondaries not only at the left and right edges, but also at the top and bottom edges, forming a completely closed structure. In this system, clockwise modes localized on the left and right edges may appear as shown in Fig. 5(a), which may generate OAM. However, by providing reflective boundaries on the top and bottom as well, counterclockwise modes are also possible as shown in Fig. 5(b). As far as we know, OAM generation has not been demonstrated using NHSE. First, we performed eigenmode calculations in a square structure with PECs on the top, bottom, left, and right edges of the $\mathcal{MT}$ symmetric medium, same as in the previous section, as shown in Fig. 5(c). Here, the x-directional width of the structure, L_x, is the same value as before, and $L_y(=L_x)$ represents the y-directional width of the structure. For the evaluation of the circulating modes, we also calculate the z component of the orbital angular momentum per photon [27]:

$$\mathrm{OAM} = \mathrm{Im}\left(\frac{\iint \boldsymbol{E}^* \cdot \frac{\partial}{\partial\phi}\boldsymbol{E}\, dxdy}{\iint \boldsymbol{E}^* \cdot \boldsymbol{E}\, dxdy}\right), \tag{11}$$

where $\boldsymbol{E}$ is the transverse electric field and ϕ is the azimuth angle.

The H_z distribution of eigenmodes are shown in Fig. 6(a) up to the 12th-order mode. The skin modes appear simultaneously at the top, bottom, left, and right edges, which is particularly noticeable for the second, fifth, eighth, 11th, and 12th modes. The direction of propagation is $+y$ for the left edge and $-y$ for the right edge, and the overall direction is clockwise. Similarly, the skin mode propagates in the $-x$ direction at the top edge and in the $+x$ direction at the bottom edge, and the overall direction is counterclockwise. A video of the propagation of mode 8 in particular is shown in Supplemental Material 1 [34]. In the square structure, these rotations are balanced and the net OAM is zero.

Here, we estimate the effective wavelength λ_{eff}, where we define λ_{eff} as twice the distance between nodes in the propagation direction of the skin mode, as shown in the 12th mode in Fig. 4(a). The effective wave number is obtained as

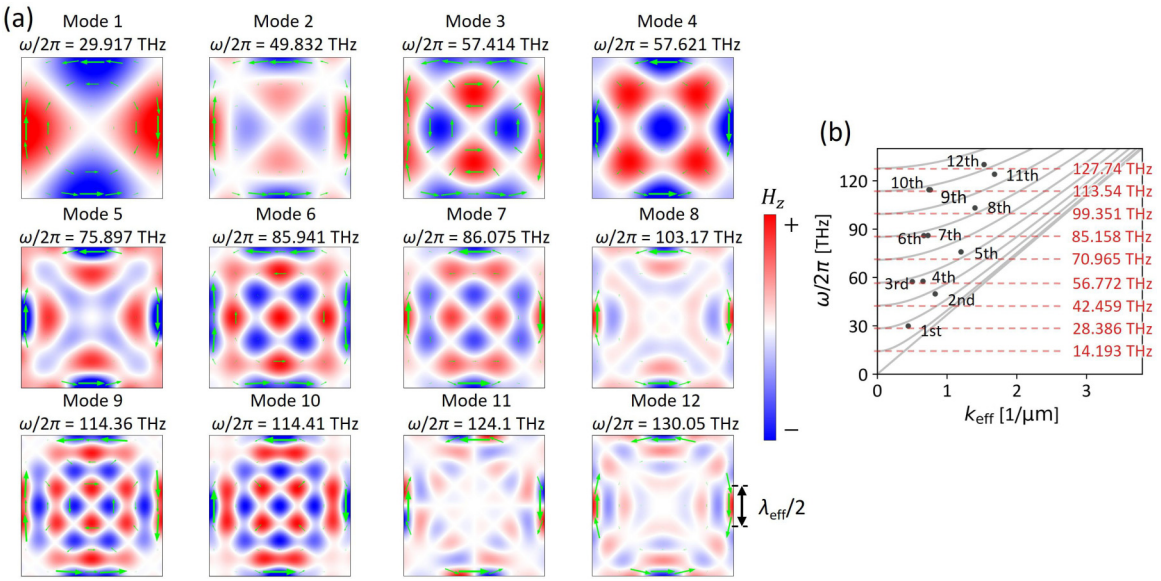

FIG. 6. (a) H_z distribution of eigenmodes from first to 12th order in square structures. Green arrows show time-averaged Poynting vectors. (b) The relationship between k_{eff} and $\omega/2\pi$ for the modes of orders 1 to 12. The gray lines show the relationship between k_y and $\omega/2\pi$ in the stripe system. The red dashed lines show the frequencies at which $k_y = 0$.

$k_{\mathrm{eff}} = 2\pi/\lambda_{\mathrm{eff}}$, and is plotted over the k_y-$\omega/2\pi$ relation in the stripe system [Fig. 3(d)] in Fig. 6(b). It can be seen that the relationship between k_{eff} and $\omega/2\pi$ is almost distributed along the frequency dispersion of the stripe system. Therefore, skin modes corresponding to the eigenmodes in the stripe system are expected to appear in the finite system as well. Indeed, corresponding to the fact that the localization of eigenmodes of the stripe system becomes stronger as k_y is larger due to the term $e^{iqk_y x}$ in Eqs. (4)–(6), the localization is stronger in the second, fifth, eighth, 11th, and 12th modes where k_{eff} is large. Here, since $q = 0.5774i$, the localization lengths of the second, fifth, eighth, 11th, and 12th modes are obtained from each k_{eff} as $|1/\mathrm{Im}(qk_{\mathrm{eff}})| = 2.09$, 1.44, 1.24, 1.03, and 1.13 μm, respectively. These are roughly consistent with the distribution of H_z obtained from the simulation.

Furthermore, from Eq. (3), the frequency at which $k_y = 0$, i.e., the eigenmode is delocalized in the stripe system, is obtained as $(c\sqrt{\eta_{yy}}/2L_x)n = 14.193n$ THz. Figure 6(a) shows that the localization is weaker in the eigenmodes at frequencies near $14.193n$ THz. This is also a confirmation that the modes corresponding to the stripe system appear in the finite system.

B. Numerical results for closed rectangular structures

Next, we performed the eigenmode calculations with a rectangular structure with $L_y = 2L_x$ in order to break the balance between clockwise and counterclockwise rotation. Some of the modes with particularly strong localization are shown in Fig. 7(a). In this case, only clockwise modes localized at the left and right boundaries strongly appear, successfully breaking the rotation balance (a video of mode 17 in particular is in Supplemental Material 2 [34]). This also resulted in a nonzero finite value of OAM. As in the square case, modes with weak localization appeared at frequencies around $14.193n$ THz, resulting in small values of OAM as shown in Fig. 7(b). In some modes, such as mode 12 in Fig. 7(b), the OAM was negative, which will be discussed later.

Now consider the case where $L_x \sim 7.07$ μm is fixed and L_y is varied. The results of plotting the relationship between eigenfrequencies and OAM for each L_y/L_x are shown in Figs. 8(a)–8(d). For a square ($L_y/L_x = 1$), the all OAMs are zero, but as L_y/L_x increases, the OAMs increase, and it is found that the OAMs saturate around $L_y/L_x = 5$. The increase in OAM with L_y/L_x is caused by the fact that in closed structures skin modes corresponding to eigenmodes in the stripe system appear. As in the case of the square structure, we estimated the effective wavelength λ_{eff} and the effective wave number k_{eff} for $L_y/L_x = 5$, and plotted the k_{eff}-$\omega/2\pi$ relationship in Fig. 8(e). Each point is almost distributed along the k_y-$\omega/2\pi$ curve in the stripe system, which is especially noticeable in the region where k_{eff} is small, indicating that the skin mode in the closed system corresponds to the skin mode in the stripe system. In addition, the distribution of $\omega/2\pi$-OAM in the rectangular structure has a comblike shape with OAMs periodically close to zero (shown by the black arrows in Fig. 8), which is similar to the $\omega/2\pi$-k_y relationship in the stripe system. Therefore, when we plot the k_{eff}-OAM relationship, especially for the case $L_y/L_x = 5$, we obtain a roughly linear relationship as shown in Fig. 8(f). This can be

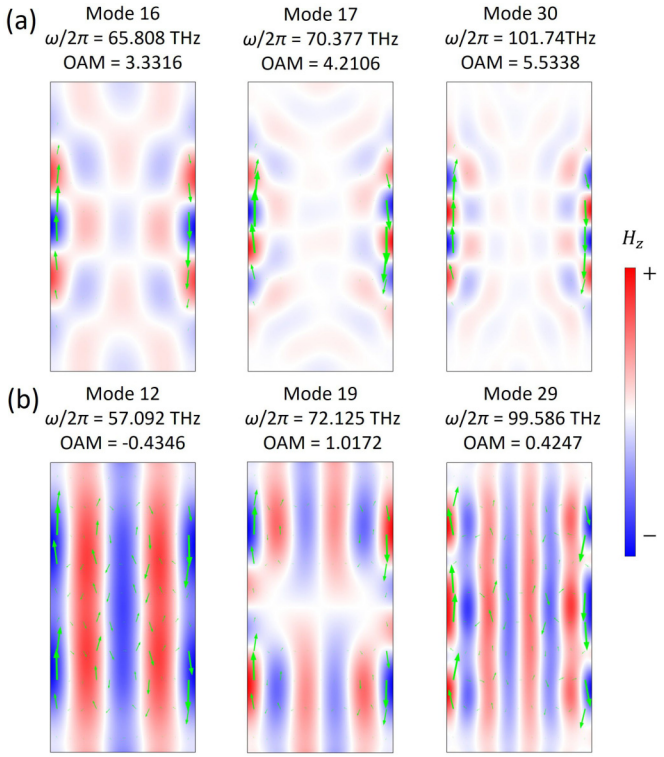

FIG. 7. H_z distribution of eigenmodes in a rectangular structure of $L_y = 2L_x$. Panel (a) shows the 16th, 17th, and 30th modes as examples of strongly localized modes. Panel (b) shows the 12th, 19th, and 29th modes as examples of weakly localized modes. Green arrows show time-averaged Poynting vectors.

understood from the definition of OAM in Eq. (11), which is equivalent to counting the number of phase windings of the electric field around the origin. Since the azimuthal phase variation is given by the product of the wave number and the displacement in the azimuthal direction, the OAM should be proportional to the effective wave number of the circulating mode for a fixed structure size. Although the propagation direction of the skin mode in a rectangular structure does not perfectly align with the azimuthal direction, leading to some deviation, the OAM is still expected to be nearly proportional to the effective wave number.

Here, skin modes at the left and right edges are formed by repeated reflections at the left and right edges while the light undergoes anisotropic loss or gain. Thus, in a structure with small L_y/L_x, when k_{eff} is large, skin modes cannot be formed at the left and right edges, limiting the value of k_{eff} that can be taken. When L_y/L_x is large, skin modes can be formed on the left and right edges even when k_{eff} is large. Therefore, as the aspect ratio of the structure is increased, the OAM proportional to k_{eff} is also expected to increase.

Moreover, when the aspect ratio becomes high enough, skin modes corresponding to eigenmodes at any points on the frequency dispersion of the stripe system [Fig. 3(d)] can be formed. As mentioned above, the skin mode in the closed system corresponds to the skin mode in the stripe system. Therefore, no matter how much the aspect ratio of the rectangle is increased, modes with wave numbers in the area below

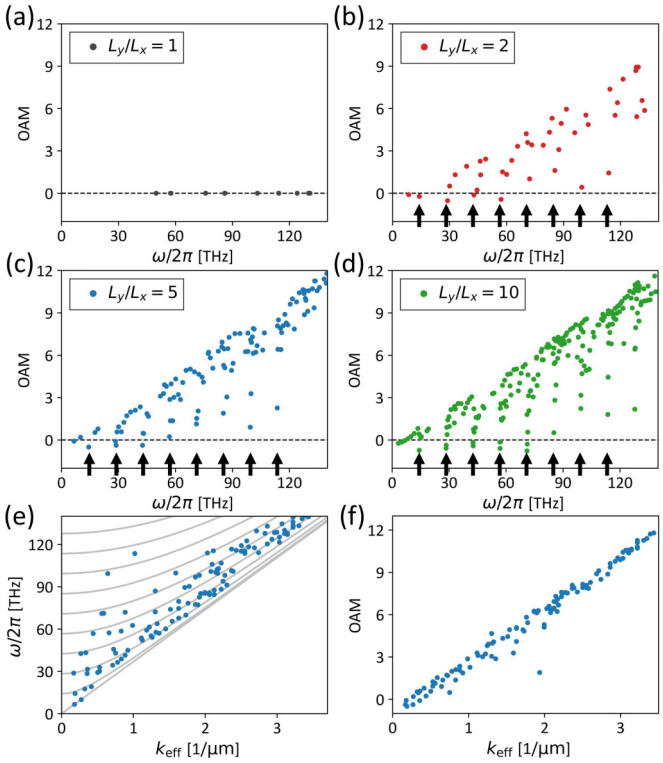

FIG. 8. [(a)–(d)] Relationship between calculated eigenfrequencies $\omega/2\pi$ and OAM for $L_y/L_x = 1, 2, 5$, and 10, respectively. In (b)–(d), the frequencies at which the OAM is close to zero are indicated by black arrows. (e) Relationship between the effective wave number k_{eff} and $\omega/2\pi$. The gray lines show the relationship between k_y and $\omega/2\pi$ in the stripe system. (f) Relationship between k_{eff} and OAM.

the $n = 0$ line in Fig. 3(d) will not appear, k_{eff} will saturate, and the OAM proportional to k_{eff} will also saturate.

Now we discuss the fact that the OAM is negative in some modes, as can be seen in Figs. 8(b)–8(d). As mentioned above, OAM and k_{eff} are proportional, and when OAM is small, k_{eff} is also small. This results in a smaller contribution from the clockwise wave traveling along the edge. Instead, the contribution of counterclockwise traveling waves inside the medium becomes relatively larger (see a video in Supplemental Material 3 [34]). Therefore, the value of OAM becomes negative in some cases close to the zero-k_{eff} condition.

C. Generation of high-efficiency circulating mode

Next, we explore the generation of more efficient circulating modes. To evaluate the efficiency of the OAM, we define the efficiency e as

$$e = \frac{\mathrm{OAM}}{N}, \tag{12}$$

where N denotes the total number of clockwise phase windings of the circulating mode around the origin. In rectangular and square structures, it is not trivial to evaluate the phase winding; thus we estimate N by

$$N = \frac{L}{\lambda_{\mathrm{eff}}}, \tag{13}$$

where L is the perimeter of the structure. Here, for an ideal circulating mode such as the Laguerre-Gaussian mode [35], the OAM efficiency is $e = 1$. As an example, the efficiency at mode 30 of rectangular structure with $L_y/L_x = 2$ [Fig. 7(a)] is calculated to be $e = 0.4246$. This is a mode with higher efficiency in the rectangular structure, but still low. Here, we seek a structure that can achieve higher efficiencies.

First, instead of breaking the equivalence of edge lengths as in the rectangular structure, we break the equivalence of interface types as shown in Fig. 9(a) and perform eigenmode calculations in a square $\mathcal{MT}$ symmetric medium sandwiched between Au layers in the x direction and Si layers in the y direction. We refer to this structure as a type I structure. The calculated H_z distribution is shown in Fig. 9(f). In this case, as in the rectangular structure, the left-right-localized clockwise modes appear strongly and OAM is generated. Here, the efficiency of the OAM is $e = 0.4963$, which is higher than that of the rectangular structure.

Next, as shown in Fig. 9(b), we performed calculations with an isosceles right triangle structure and found that skin modes do not appear on the diagonal edges, and skin modes propagating in the $+y$ direction appear only on the perpendicular edges. Here, this 45° diagonal edge is parallel to the mirror symmetry plane of the dielectric tensor. The fact that skin modes do not appear on the edge parallel to the mirror symmetry plane of the system is known as a property of the geometry-dependent skin effect (GDSE) [28]. This is a type of NHSE in fully closed boundary systems, and GDSE is thought to be appearing in the medium used in this study. Therefore, to generate a one-directional circulation along the edges, we designed the type II structure, as shown in Fig. 9(c). This structure is constructed by dividing a uniform square medium [Fig. 5(c)] along both 45° diagonals and horizontally flipping the upper and lower regions with respect to the vertical axis. Thus the anisotropy orientations differ between the vertical and horizontal edges. Similar to how edge equivalence is broken in rectangular or type I structures—through edge lengths or interface materials—this anisotropy mismatch breaks the equivalence of vertical and horizontal edges and a directional circulation of skin modes is therefore expected to appear.

The calculated H_z distribution for this structure is shown in Fig. 9(g). We succeeded in generating skin modes that circulate not only on the left and right edges but also around the perimeter in one direction. Even when the structures are combined, the properties of GDSE are considered valid, and we expect that the one-directional circulation localized only on the perimeter of such a structure is obtained. Also, in this case, the efficiency of the OAM is $e = 0.6181$, which is higher than that of type I structure. In addition, because of the nature of GDSE, the conditions for skin modes to appear is satisfied except at 45° diagonal edges. Thus we also designed the type III structure shown in Fig. 9(d), which is a circular counterpart of the type II structure, where the anisotropy orientation differs between the left-right and upper-lower regions. In this structure, $e = 0.8108$ is obtained, which is a higher efficiency than that of the circulating mode in type II structure.

In addition, we calculated in the circular structure with anisotropic dielectric permittivity with $\mathcal{MT}$ symmetric anisotropy continuously rotated around the center of the circle, as shown in Fig. 9(e). Each component of the dielectric

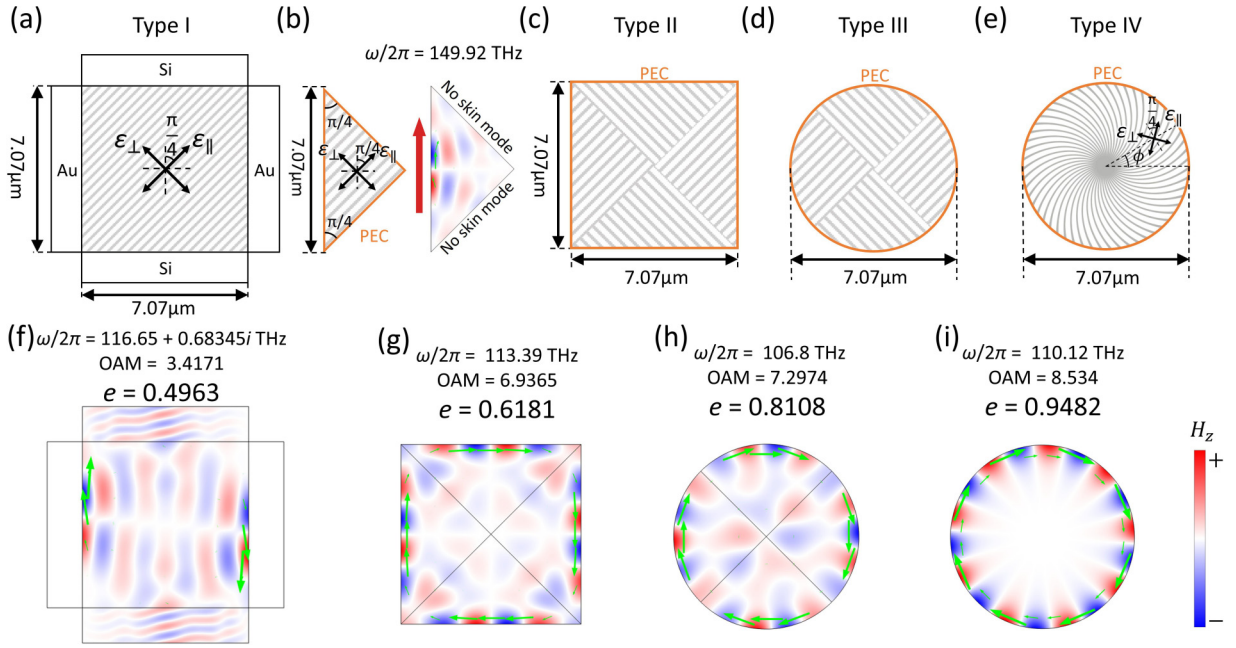

FIG. 9. (a) Square $\mathcal{MT}$ symmetric medium sandwiched between Au layers in the x direction and Si layers in the y direction. (b) Isosceles right triangular $\mathcal{MT}$ symmetric medium and the eigenmodes in this structure. (c) Structure consisting of four triangular $\mathcal{MT}$ symmetric media in (b). (d) Circular structure consisting of four fan-shaped $\mathcal{MT}$ symmetric media. (e) Circular structure consisting of four fan-shaped $\mathcal{MT}$ symmetric media. The dielectric constants are $\varepsilon_{xx} = \varepsilon_\perp \cos^2(\phi - \pi/4) + \varepsilon_\parallel \sin^2(\phi - \pi/4)$, $\varepsilon_{yy} = \varepsilon_\perp \sin^2(\phi - \pi/4) + \varepsilon_\parallel \cos^2(\phi - \pi/4)$, $\varepsilon_{xy} = \varepsilon_{yx} = (\varepsilon_\perp - \varepsilon_\parallel)\sin(\phi - \pi/4)\cos(\phi - \pi/4)$, where $\varepsilon_\parallel = 1.673 + 0.965\,93i$, $\varepsilon_\perp = 1.673 - 0.965\,93i$. (f)–(i) Eigenmodes in the structures (a),(c)–(e), respectively. Green arrows show time-averaged Poynting vectors.

constant tensor is $\varepsilon_{xx} = \varepsilon_\perp \cos^2(\phi - \pi/4) + \varepsilon_\parallel \sin^2(\phi - \pi/4)$, $\varepsilon_{yy} = \varepsilon_\perp \sin^2(\phi - \pi/4) + \varepsilon_\parallel \cos^2(\phi - \pi/4)$, $\varepsilon_{xy} = \varepsilon_{yx} = (\varepsilon_\perp - \varepsilon_\parallel)\sin(\phi - \pi/4)\cos(\phi - \pi/4)$. We refer to this structure as type IV structure. In the case of the type III structure, the appearance of skin modes is weak near the point where the tangent line of the circle is 45° diagonal, due to the characteristics of GDSE. On the other hand, in the type IV structure, skin modes can exist for all angles on the circle, which is expected to result in better efficiency e. The calculated H_z distribution is shown in Fig. 9(i). In this case, as expected, a skin mode circulating in one direction appeared on the perimeter. Also, the OAM efficiency is $e = 0.9482$, which is the highest efficiency of the circulating modes in the structures considered in this section. Although this mode appears to be an ideal circulating mode, its efficiency does not reach the ideal value of 1. This is thought to be due to a slight decrease in OAM caused by the contribution of a weak counterclockwise circulation inside the structure (see video in Supplemental Material 7 [34]). The details of this and the method to obtain a higher efficiency are discussed in Appendix B.

Here, videos of the modes in Figs. 9(f)–9(h) are also shown in Supplemental Material 4–6, respectively [34].

D. Comparison of purity of circulating modes

Next, we discuss the purity of the circulating mode using the following equation [36]. Hereafter we will refer to this as the OAM spectrum.

$$F(l) = \frac{|d_l|^2}{\sum_{l'} |d_{l'}|^2}, \tag{14}$$

$$d_l = \int_0^{2\pi} \int_0^{\infty} H_z e^{-il\phi} r dr d\phi, \tag{15}$$

where l is the azimuthal mode number. l can be any integer, with positive l corresponding to a clockwise mode and negative l to a counterclockwise mode. Here the OAM spectrum is the content of each basis when H_z is expanded into a basis of $e^{il\phi}$. Note that for a pure circulating mode with a spatial distribution of the field that depends on $e^{il\phi}$ ($l \neq 0$), such as Laguerre-Gaussian mode, the OAM spectrum is $F(l) = 1$.

Figure 10 shows the results of the OAM spectrum calculations. First, for mode 8 in the square structure [Fig. 6(a)], the OAM spectrum has a symmetric distribution [Fig. 10(a)]. This corresponds to the fact that the clockwise and counterclockwise modes are in balance and the OAM is zero. Next for mode 30 in the rectangular structure [Fig. 7(a)] and the mode in type I structure [Fig. 9(a)], the left-right symmetry of the OAM spectrum is broken and the OAM spectrum is strongly distributed on the positive side of l [Figs. 10(b) and 10(c)]. This corresponds to the strong appearance of clockwise modes localized on the left and right sides. Furthermore, for the modes in type II structure [Fig. 9(g)] and type III structure [Fig. 9(h)], the variation in the distribution of the OAM spectrum is smaller, corresponding to the high OAM efficiency obtained in the previous section. In particular, it is more pronounced for type III structure. The mode in type

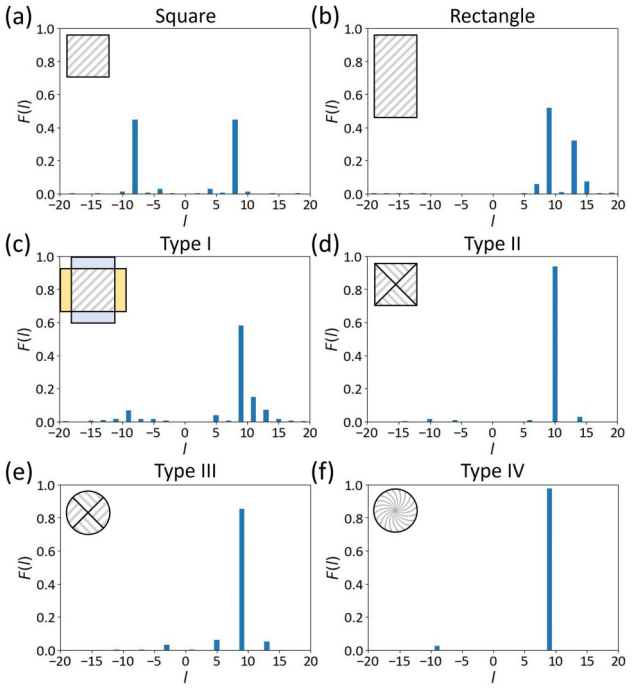

FIG. 10. [(a)–(f)] OAM spectrum of mode 8 in Fig. 6(a), mode 30 in Fig. 7(a), and modes shown in Figs. 9(f)–9(i), respectively. A schematic of the structure is shown in the upper left corner of each graph.

IV structure [Fig. 9(i)] shows the smallest variation in the distribution of the OAM spectrum and the highest purity. This is also consistent with the highest efficiency obtained in the previous section for this structure.

V. CIRCULATING SKIN MODES IN LOSS-BIASED CASE

So far, we have considered circulating modes in a medium in which gain and loss are balanced. However, it is difficult to realize a medium with large gain and balanced gain and loss in a real material. In this section, we consider circulating modes in loss-biased media with a view to demonstrating them experimentally. Here, as in Fig. 11(a), we use an anisotropic loss-biased medium with dielectric constants $\varepsilon_{xx} = \varepsilon_{yy} = 1.673 - 0.965\,93i$ and $\varepsilon_{xy} = \varepsilon_{yx} = -0.965\,93i$, given by Eq. (10), $\varepsilon_{\parallel} = 1.673$, and $\varepsilon_{\perp} = 1.673 - 1.931\,86i$. These are obtained by increasing the loss while holding the contrast of the imaginary part of the $\mathcal{MT}$ symmetric dielectric constants ($\varepsilon_{\parallel} = 1.673 + 0.965\,93i$ and $\varepsilon_{\perp} = 1.673 - 0.965\,93i$) that we have used. Then we will replace the structures in the previous section with this medium.

Figures 11(b)–11(d) show the calculated H_z distributions for each structure. Note that these are the modes whose effective wave numbers are close to those of mode 8 in Fig. 6, mode 30 in Fig. 7, and the modes in Figs. 9(f)–9(i), respectively. First, in the square structure, clockwise modes localized on the left and right edges and counterclockwise modes localized on the top and bottom edges appeared simultaneously, and

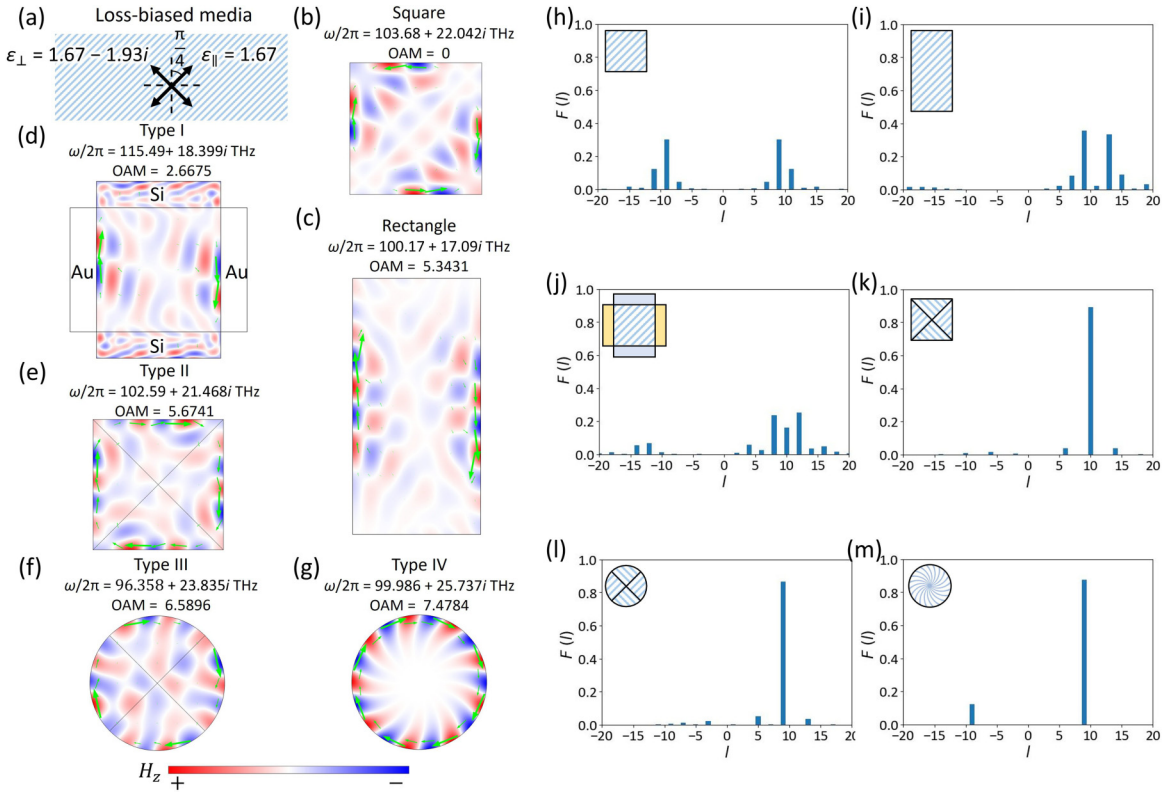

FIG. 11. (a) Schematic of loss-bias media. [(b)–(g)] The eigenmodes in the square structure, the rectangular structure ($L_y/L_x = 2$), the structure sandwiched between Au and Si layers, the structure combining right triangle, the structure combining fan shape, and the structure with continuously rotated anisotropy around the center, respectively. Green arrows show time-averaged Poynting vectors. [(h)–(m)] OAM spectra of modes shown in (b)–(g), respectively.

TABLE I. Comparison of OAM efficiency in the loss-gain balanced case and in the loss-biased case.

	Structure					
OAM efficiency e	Loss-gain balance	0.4246	0.5439	0.6181	0.8108	0.9482
	Loss bias	0.3803	0.4316	0.5599	0.7322	0.8309

they were in balance, resulting in zero OAM [Fig. 11(b)]. Corresponding to this, the OAM spectrum was symmetrically distributed [Fig. 11(h)]. Next, in the rectangular structure ($L_y/L_x = 2$) and type I structure, clockwise modes strongly appeared [Figs. 11(c) and 11(d)], and the OAM spectrum was asymmetric [Figs. 11(i) and 11(j)].

In addition, in type II–IV structures, a circulating mode traveling in one direction around the perimeter of the structure appears [Figs. 11(e)–11(g)], and the variation of the OAM spectrum is smaller than that of the rectangular and type I structures [Figs. 11(k)–11(m)]. In particular, type IV structure has the purest circulating mode with the smallest variation of the OAM spectrum of the modes in the square, rectangle, and type I–IV structures. These are the same trends as when using $\mathcal{MT}$ symmetric media.

Also, the calculated efficiencies of the OAM for each structure are shown in Table I. Note that the efficiencies in the $\mathcal{MT}$ symmetric case are also shown for comparison. This shows that the efficiency increases in the order of the rectangular, and types I, II, III, and IV structures, which is also the same trend as in the $\mathcal{MT}$ symmetric case.

Then we compare the OAM efficiency in the $\mathcal{MT}$ symmetric case and the loss-biased case. Table I shows that for each structure, the OAM efficiency in the loss-biased case is lower than in the $\mathcal{MT}$ symmetric case. This reduction is slight for the loss introduced, suggesting that it is easy to realize. Here, possible reasons for this decrease in efficiency are, first, the imbalance between loss and gain, which tilts the propagation direction of the circulating mode toward the azimuthal direction, and second, the longer localization length of the skin mode than in the $\mathcal{MT}$ symmetric case, which increases its contribution to the counterclockwise circulation, resulting in a decrease in net OAM. We discuss this in detail in Appendixes C and D.

As described above, OAM is feasible even with a loss-biased medium. The OAM and OAM spectral features for each structure were similar to those obtained with $\mathcal{MT}$ symmetric media, and the OAM decrease was slight for the introduced loss. However, the imaginary part of the eigenfrequencies increases.

VI. SUMMARY AND DISCUSSION

We have investigated numerically the propagation of NHSE in two-dimensional reciprocal uniform media. In the simulation of the propagation of skin modes with the $\mathcal{MT}$ symmetric medium, we found an interesting phenomenon: the skin modes jump between opposite edges due to scattering and travel in opposite directions to each other.

Applying this interedge coupling, we have investigated a square structure surrounded by PECs. We found that clockwise modes localized on the left and right edges and counterclockwise modes localized on the top and bottom edges appeared simultaneously, and the OAM became zero by balancing them. However, in a rectangular structure or a structure sandwiched between different media, such as Au layers on the left and right and Si layers on the top and bottom, one rotation was selectively exhibited and a nonzero OAM was obtained. In other words, finite OAM can be generated by breaking the balance between the horizontal and vertical boundaries. In addition, we confirmed that high efficiency and high purity circulating modes can be achieved in structures where the anisotropy orientation differs between the left-right and upper-lower regions, such as in the type II and III structures. We examined these structures inspired by the fact that skin modes do not appear at the 45° diagonal edges in the right triangle structure. In Ref. [28], the geometry dependence of the skin state in two-dimensional lattice models is discussed. As a property of geometry-dependent NHSE (GDSE), the skin state appearing at each edge in a fully closed system corresponds to the skin state in an infinitely long stripe geometry parallel to that edge and the skin state does not appear on edges parallel to the mirror symmetry plane of the system. The former property was discussed in Secs. IV A and IV B and the latter in Sec. IV C. Thus it can be assumed that GDSE is also appearing in the system we have considered. Therefore, our results confirm that application of GDSE as the OAM generation. As far as we know, there has been no demonstration of OAM generation from NHSE. Furthermore, we considered a medium with continuously rotating anisotropy and obtained the most efficient and purest circulating modes.

We also replaced the medium with an anisotropic loss-biased medium and performed the same calculations and found that the circulating mode can still be generated in this case. This result suggests experimental demonstrability since, unlike the $\mathcal{MT}$ symmetric medium, no gain is required to construct this medium and it is easy to realize. Our work also paves the way for the application of NHSE as microsized optical devices manipulating OAM, such as OAM light emitters and OAM-dependent transmission or reflection devices.

ACKNOWLEDGMENTS

This work was supported by the Japan Society for the Promotion of Science (Grants No. JP20H05641, No. JP21K14551, No. 24K01377, No. 24H02232, and No. 24H00400).

DATA AVAILABILITY

The data that support the findings of this article are openly available [37]; embargo periods may apply.

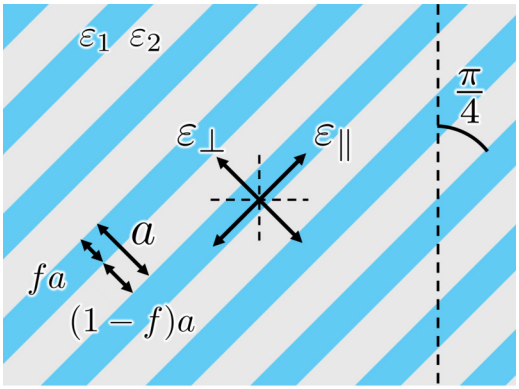

FIG. 12. Schematic of multilayer structure.

APPENDIX A: COMPOSITION OF $\mathcal{MT}$ SYMMETRIC DIELECTRIC CONSTANTS WITH MULTILAYERS

In this section, we consider composing $\mathcal{MT}$ symmetric dielectric constants with multilayers. We consider a multilayer structure tilted by 45° as shown in Fig. 12, where a is the lattice constant, ε_1 is the dielectric constant of medium 1, ε_2 is the dielectric constant of medium 2, and f is the ratio of the thickness of medium 1 to the lattice constant a. When a is sufficiently shorter than the wavelength of light, by the effective medium approximation, the dielectric constants $\varepsilon_\parallel$ in the direction parallel to the multilayer and $\varepsilon_\perp$ in the direction perpendicular to it can each be expressed as follows:

$$\varepsilon_\parallel = f\varepsilon_1 + (1-f)\varepsilon_2, \quad \varepsilon_\perp = \frac{\varepsilon_1\varepsilon_2}{(1-f)\varepsilon_1 + f\varepsilon_2}. \tag{A1}$$

Here, the dielectric constants of media1 and 2 are written as

$$\varepsilon_1 = A_1 e^{i\phi_1}, \quad \varepsilon_2 = A_2 e^{i\phi_2}\ (-\pi < \phi_1, \phi_2 < \pi). \tag{A2}$$

Then we find the conditions for A_1, A_2, ϕ_1, and ϕ_2 under which the $\mathcal{MT}$ symmetry holds. As mentioned in Sec. II A, $\mathcal{MT}$ symmetry is satisfied when $\varepsilon_\parallel = \varepsilon_\perp^*$. Substituting Eq. (A2) into this equation and multiplying both sides by $(1-f)\varepsilon_1 + f\varepsilon_2$, we obtain the following equation:

$$f(1-f)(|\varepsilon_1|^2 + |\varepsilon_2|^2) + f^2\varepsilon_1^*\varepsilon_2 + (1-f)^2\varepsilon_1\varepsilon_2^* = \varepsilon_1^*\varepsilon_2^*. \tag{A3}$$

Substituting Eq. (A2) and considering the imaginary part, we obtain

$$\begin{aligned} &-f^2A_1A_2\sin(\phi_1-\phi_2) + (1-f)^2A_1A_2\sin(\phi_1-\phi_2) \\ &\quad = -A_1A_2\sin(\phi_1+\phi_2). \end{aligned} \tag{A4}$$

By rearranging this equation, the condition on ϕ_1, ϕ_2 can be obtained as

$$\phi_2 = \tan^{-1}\left(\frac{f-1}{f}\tan\phi_1\right). \tag{A5}$$

Since $(f-1)/f < 0$, $\mathrm{sign}(\phi_1) \neq \mathrm{sign}(\phi_2)$. Thus we can confirm that both gain and loss media are required to compose $\mathcal{MT}$ symmetric dielectric constants by the effective medium approximation of the multilayer. Next, considering the real part of Eq. (A3), we obtain

$$\begin{aligned} &f(1-f)\left(A_1^2 + A_2^2\right) + f^2A_1A_2\cos(\phi_1-\phi_2) \\ &\quad +(1-f)^2\cos(\phi_1-\phi_2) = A_1A_2\cos(\phi_1+\phi_2). \end{aligned} \tag{A6}$$

By rearranging this equation, the conditions on A_1 and A_2 are given by

$$A_2 = \frac{1}{2}(X \pm \sqrt{X^2-4})A_1, \tag{A7}$$

$$X = \frac{\cos(\phi_1+\phi_2) - [f^2 + (1-f)^2]\cos(\phi_1-\phi_2)}{f(1-f)}. \tag{A8}$$

In particular, considering the case $f = 1/2$, from Eq. (A5), $\phi_2 = -\phi_1$. Furthermore, by setting $\phi_2 = -\phi_1 = \pi/4, A_1 = 1$, and $A_2 = 2+\sqrt{3}$, the dielectric constants of each medium are obtained as $\varepsilon_1 = 0.707\,11 - 0.707\,11i$ and $\varepsilon_2 = 2.639 + 2.639i$. With this and Eq. (A1), we obtain the $\mathcal{MT}$ symmetric dielectric constants $\varepsilon_\parallel = \varepsilon_\perp^* = 1.673 + 0.965\,93i$ used in this paper.

The width $L_x \sim 7.07$ μm of the structure used in this paper corresponds to 25 periods of multilayers when the lattice constant is $a = 0.2$ μm.

APPENDIX B: DEPENDENCE OF OAM EFFICIENCY ON THE STRENGTH OF NON-HERMITICITY IN THE TYPE IV STRUCTURE

In Sec. IV C, we stated that the OAM efficiency of the mode in the type IV structure does not reach 1 due to the contribution of a counterclockwise circulation. This counterclockwise circulation originates from the insufficient strength of the anisotropic gain and loss.

Here, we define the dielectric constants $\varepsilon_\parallel$ and $\varepsilon_\perp$ in the type IV structure as

$$\varepsilon_\parallel = 1.673 + i\varepsilon_{\mathrm{Im}}, \quad \varepsilon_\perp = 1.673 - i\varepsilon_{\mathrm{Im}}. \tag{B1}$$

The imaginary part $\varepsilon_{\mathrm{Im}}$ determines the strength of anisotropic gain and loss. Figure 13(a) shows the relationship between $\varepsilon_{\mathrm{Im}}$ and the OAM efficiency e. It indicates that the efficiency converges to 1 as $\varepsilon_{\mathrm{Im}}$ increases. In the following, we discuss the background of this behavior.

First, we consider the case of $\varepsilon_{\mathrm{Im}} = 0$. In this situation, $\varepsilon_\parallel = \varepsilon_\perp = 1.673$, and the medium becomes isotropic. (Hereafter, we set $\varepsilon = 1.673$.) The magnetic field component H_z of a TE mode in such an isotropic circular cavity can be found analytically by solving the Helmholtz equation in a cylindrical coordinate system as

$$H_z(r,\phi) = AJ_u(k_{uv}r)(e^{iu\phi} \pm e^{-iu\phi}), \tag{B2}$$

$$k_{uv}^2 = \varepsilon\omega_{uv}^2/c^2, \tag{B3}$$

where A is a constant, u is the azimuthal mode number, v is the radial mode number, J_u is the Bessel function of the first kind, and ω_{uv} is the eigenfrequency. Furthermore, the wave number k_{uv} must satisfy the following condition due to the PEC boundary condition:

$$J_u'(k_{uv}R) = 0, \tag{B4}$$

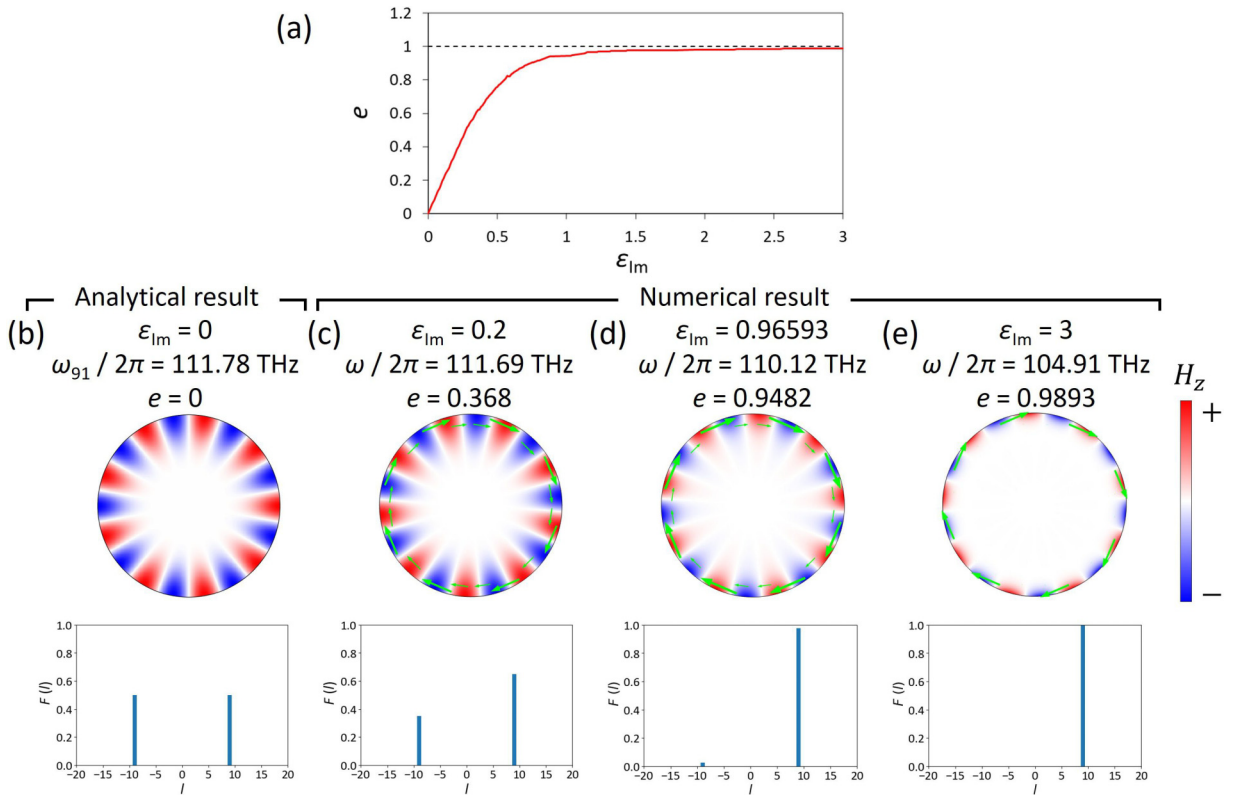

FIG. 13. (a) The relationship between the imaginary part of the dielectric constants $\varepsilon_{\mathrm{Im}}$ and the efficiency e. [(b),(c)] The eigenmodes and the OAM spectra for the type IV structure with $\varepsilon_{\mathrm{Im}} = 0.965\,93$ and 3, respectively. Green arrows show time-averaged Poynting vectors.

where R is the radius of the structure. This solution forms a standing wave composed of a $+u$-order clockwise wave and a $-u$-order counterclockwise wave with equal amplitudes. Figure 13(b) shows the analytical solution for the case of $u = 9$ and $v = 1$. The spectrum has balanced peaks at $l = \pm 9$, and the net OAM is zero.

Next, when a nonzero $\varepsilon_{\mathrm{Im}}$ is introduced, the anisotropic gain and loss selectively suppress the counterclockwise circulation, which results in a nonzero OAM. When the value of $\varepsilon_{\mathrm{Im}}$ is small [Fig. 13(c)], this suppression is insufficient and a residual counterclockwise component remains, which lowers the OAM and consequently results in a small efficiency e. For the value used in this paper, $\varepsilon_{\mathrm{Im}} = 0.965\,93$ [Fig. 13(d)], the counterclockwise component is significantly suppressed, but a small amount remains, preventing the efficiency from reaching 1. As $\varepsilon_{\mathrm{Im}}$ is further increased [Fig. 13(e)], the counterclockwise component is almost completely eliminated, and the OAM spectrum approaches a single peak. As a result, the OAM efficiency e converges to the ideal value of 1. Furthermore, when $\varepsilon_{\mathrm{Im}}$ is large, it can be seen that the localization due to the skin effect also becomes prominent.

It should be noted that while Fig. 13 shows only one representative mode for each case, the solutions are paired. For the $\varepsilon_{\mathrm{Im}} = 0$ case, the clockwise and counterclockwise circulating modes are degenerate. As indicated by the analytical solution in Eq. (B2), this yields two distinct standing-wave modes with OAM $= 0$. Similarly, in our numerical results for the $\varepsilon_{\mathrm{Im}} \neq 0$ case, two modes are consistently estimated as a pair, possessing the same eigenfrequency and net OAM.

APPENDIX C: TILT OF THE WAVE FRONT OF THE SKIN MODE IN THE LOSS-BIASED CASE

In this section, we explain the tilt of the wave front of the skin mode in the loss-biased case. First, for a system sandwiched by PECs in the x direction and periodic in the y direction, from Eqs. (4)–(6), each component of the electromagnetic field can be expressed in the following form:

$$F(x) = e^{iqk_y x} f(x). \tag{C1}$$

Here, as confirmed in Sec. II B, in an $\mathcal{MT}$ symmetric medium, q in Eq. (7) is pure imaginary, so we write $q = iq_{\mathrm{I}}$. Then,

$$F(x, y, t) = e^{i(\omega t - k_y y)} e^{-q_{\mathrm{I}} k_y x} f(x), \tag{C2}$$

and the state is localized in the x direction but traveling in the y direction. In the loss-biased case, on the other hand, q is complex and can be written as $q = q_{\mathrm{R}} + iq_{\mathrm{I}}$, where $q = 0.25 + 0.433i$ when $\varepsilon_{\parallel} = 1.673$ and $\varepsilon_{\perp} = 1.673 - 1.931\,86i$. In this case, the electromagnetic field is

$$F(x, y, t) = e^{i(\omega t + q_{\mathrm{R}} k_y x - k_y y)} e^{-q_{\mathrm{I}} k_y x} f(x) \tag{C3}$$

and thus the wave front of the skin mode is tilted. Since it is the component traveling in the azimuthal direction that contributes to OAM, in the loss-biased case, the tilt of the wave front may lead to a decrease in OAM.

APPENDIX D: RELATIONSHIP BETWEEN LOCALIZATION LENGTH OF SKIN MODE AND OAM

In this section, we discuss the relationship between the localization length of the skin mode and OAM. First, we consider the case where the localization length of the skin mode is sufficiently short (Fig. 14). In this case, the skin mode propagation contributes only to unidirectional circulation. However, as shown in Fig. 14, when the localization length is long, the tail of the skin mode will contribute to rotation in the opposite direction. This would result in a smaller OAM than in the case of shorter localization lengths.

From Eqs. (4)–(6), q in Eq. (7) is one of the quantities that determine the localization length, and when compared for skin modes with the same k_y, the larger $|\mathrm{Im}(q)|$ is, the shorter the localization length becomes. Here, in the $\mathcal{MT}$ symmetric medium used in Sec. IV, $|\mathrm{Im}(q)| = 0.5774$, and in the loss-biased medium used in Sec. V, $|\mathrm{Im}(q)| = 0.4473$. Thus, when compared for similar order modes, the localization length is longer in the loss-biased case. This may also be one of the reasons for the lower OAM shown in Sec. V.

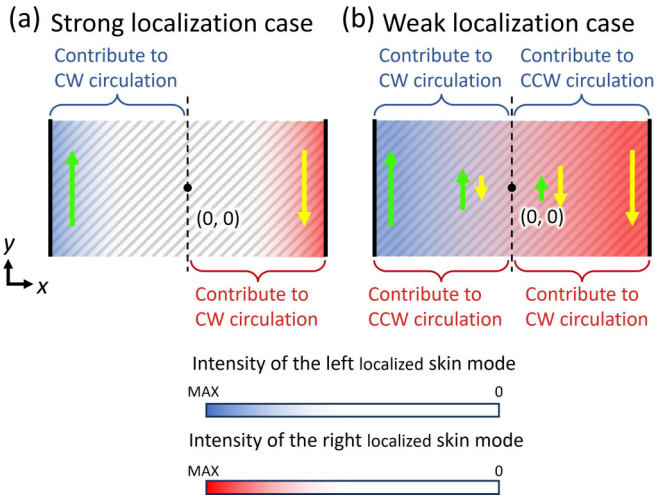

FIG. 14. [(a),(b)] Contribution of skin mode to rotation for short and long localization lengths, respectively. Blue and red represent the intensity of the left- and right-localized skin modes, respectively, and green and yellow arrows represent the Poynting vectors of the left- and right-localized skin modes, respectively.

[1] C. M. Bender and S. Boettcher, Real spectra in non-Hermitian Hamiltonians having $\mathcal{PT}$ symmetry, Phys. Rev. Lett. **80**, 5243 (1998).

[2] H. Ramezani, T. Kottos, R. El-Ganainy, and D. N. Christodoulides, Unidirectional nonlinear $\mathcal{PT}$-symmetric optical structures, Phys. Rev. A **82**, 043803 (2010).

[3] B. Peng, S. Ozdemir, F. Lei, F. Monifi, M. Gianfreda, G. Long, S. Fan, F. Nori, C. Bender, and L. Yang, Parity–time-symmetric whispering-gallery microcavities, Nat. Phys. **10**, 394 (2014).

[4] L. Chang, X. Jiang, S. Hua, C. Yang, J. Wen, L. Jiang, G. Li, G. Wang, and M. Xiao, Parity–time symmetry and variable optical isolation in active–passive-coupled microresonators, Nat. Photon. **8**, 524 (2014).

[5] Z. Lin, H. Ramezani, T. Eichelkraut, T. Kottos, H. Cao, and D. N. Christodoulides, Unidirectional invisibility induced by $\mathcal{PT}$-symmetric periodic structures, Phys. Rev. Lett. **106**, 213901 (2011).

[6] A. Regensburger, C. Bersch, M.-A. Miri, G. Onishchukov, D. N. Christodoulides, and U. Peschel, Parity-time synthetic photonic lattices, Nature (London) **488**, 167 (2012).

[7] L. Feng, Y.-L. Xu, W. S. Fegadolli, M.-H. Lu, J. E. B. Oliveira, V. R. Almeida, Y.-F. Chen, and A. Scherer, Experimental demonstration of a unidirectional reflectionless parity-time metamaterial at optical frequencies, Nat. Mater. **12**, 108 (2013).

[8] K. Takata and M. Notomi, $\mathcal{PT}$-Symmetric coupled-resonator waveguide based on buried heterostructure nanocavities, Phys. Rev. Appl. **7**, 054023 (2017).

[9] V. M. Martinez Alvarez, J. E. Barrios Vargas, and L. E. F. Foa Torres, Non-Hermitian robust edge states in one dimension: Anomalous localization and eigenspace condensation at exceptional points, Phys. Rev. B **97**, 121401(R) (2018).

[10] S. Yao and Z. Wang, Edge states and topological invariants of non-Hermitian systems, Phys. Rev. Lett. **121**, 086803 (2018).

[11] S. Weidemann, M. Kremer, T. Helbig, T. Hofmann, A. Stegmaier, M. Greiter, R. Thomale, and A. Szameit, Topological funneling of light, Science **368**, 311 (2020).

[12] L. Xiao, T.-S. Deng, K. Wang, G. Zhu, Z. Wang, and W. Yi, Non-Hermitian bulk–boundary correspondence in quantum dynamics, Nat. Phys. **16**, 761 (2020).

[13] M. Brandenbourger, X. Locsin, E. Lerner, and C. Coulais, Non-reciprocal robotic metamaterials, Nat. Commun. **10**, 4608 (2019).

[14] A. Ghatak, M. Brandenbourger, J. Wezel, and C. Coulais, Observation of non-Hermitian topology and its bulk–edge correspondence in an active mechanical metamaterial, Proc. Natl. Acad. Sci. USA **117**, 29561 (2020).

[15] Y. Chen, X. Li, C. Scheibner, V. Vitelli, and G. Huang, Realization of active metamaterials with odd micropolar elasticity, Nat. Commun. **12**, 5935 (2021).

[16] T. Helbig, T. Hofmann, S. Imhof, M. Abdelghany, T. Kiessling, L. W. Molenkamp, C. H. Lee, A. Szameit, M. Greiter, and R. Thomale, Generalized bulk–boundary correspondence in non-Hermitian topolectrical circuits, Nat. Phys. **16**, 747 (2020).

[17] T. Hofmann, T. Helbig, F. Schindler, N. Salgo, M. Brzezińska, M. Greiter, T. Kiessling, D. Wolf, A. Vollhardt, A. Kabaši, C. H. Lee, A. Bilušić, R. Thomale, and T. Neupert, Reciprocal skin effect and its realization in a topolectrical circuit, Phys. Rev. Res. **2**, 023265 (2020).

[18] L. Zhang, Y. Yang, Y. Ge, Y.-J. Guan, Q. Chen, Q. Yan, F. Chen, R. Xi, Y. Li, D. Jia, S.-Q. Yuan, H.-X. Sun, H. Chen, and B. Zhang, Acoustic non-Hermitian skin effect from twisted winding topology, Nat. Commun. **12**, 6297 (2021).

[19] W. Gou, T. Chen, D. Xie, T. Xiao, T.-S. Deng, B. Gadway, W. Yi, and B. Yan, Tunable nonreciprocal quantum transport through a dissipative Aharonov-Bohm ring in ultracold atoms, Phys. Rev. Lett. **124**, 070402 (2020).

[20] J. Zhong, K. Wang, Y. Park, V. Asadchy, C. C. Wojcik, A. Dutt, and S. Fan, Nontrivial point-gap topology and non-Hermitian skin effect in photonic crystals, Phys. Rev. B **104**, 125416 (2021).

[21] Z. Fang, M. Hu, L. Zhou, and K. Ding, Geometry-dependent skin effects in reciprocal photonic crystals, Nanophotonics **11**, 3447 (2022).

[22] Q. Zhou, J. Wu, Z. Pu, J. Lu, X. Huang, W. Deng, M. Ke, and Z. Liu, Observation of geometry-dependent skin effect in non-Hermitian phononic crystals with exceptional points, Nat. Commun. **14**, 4569 (2023).

[23] K. Yokomizo, T. Yoda, and S. Murakami, Non-Hermitian waves in a continuous periodic model and application to photonic crystals, Phys. Rev. Res. **4**, 023089 (2022).

[24] W. Zhu and J. Gong, Photonic corner skin modes in non-Hermitian photonic crystals, Phys. Rev. B **108**, 035406 (2023).

[25] T. Yoda, Y. Moritake, K. Takata, K. Yokomizo, S. Murakami, and M. Notomi, Optical non-Hermitian skin effect in uniform media, Phys. Rev. Res. **7**, 033214 (2025).

[26] D. Cheng, E. Lustig, K. Wang, and S. Fan, Multi-dimensional band structure spectroscopy in the synthetic frequency dimension, Light Sci. Appl. **12**, 158 (2023).

[27] M. V. Berry, Paraxial beams of spinning light, in *Proceedings of the International Conference on Singular Optics*, Vol. 3487 (SPIE, Bellingham, WA, 1988).

[28] K. Zhang, Z. Yang, and C. Fang, Universal non-Hermitian skin effect in two and higher dimensions, Light Sci. Appl. **13**, 2496 (2022).

[29] Y.-C. Wang, J.-S. You, and H. Jen, A non-Hermitian optical atomic mirror, Nat. Commun. **13**, 4598 (2022).

[30] Z. Wang, Y. D. Chong, J. D. Joannopoulos, and M. Soljačić, Reflection-Free one-way edge modes in a gyromagnetic photonic crystal, Phys. Rev. Lett. **100**, 013905 (2008).

[31] B. Xiao, K. Lai, Y. Yu, T. Ma, G. Shvets, and S. M. Anlage, Exciting reflectionless unidirectional edge modes in a reciprocal photonic topological insulator medium, Phys. Rev. B **94**, 195427 (2016).

[32] T. Ma and G. Shvets, Scattering-free edge states between heterogeneous photonic topological insulators, Phys. Rev. B **95**, 165102 (2017).

[33] J.-P. Bérenger, *Perfectly Matched Layer (PML) for Computational Electromagnetics*, Synthesis Lectures on Computational Electromagnetics (Springer, Berlin, 2007).

[34] See Supplemental Material at http://link.aps.org/supplemental/10.1103/gqlb-qxkl for videos of mode 8 in Fig. 6(a), mode 17 in Fig. 7(a), mode 12 in Fig. 7(b), and the modes in Figs. 9(f)–9(i).

[35] L. Allen, M. Padgett, and M. Babiker, The orbital angular momentum of light, Prog. Opt. **39**, 291 (1999).

[36] Y.-D. Liu, C. Gao, M. Gao, and F. Li, Coherent-mode representation and orbital angular momentum spectrum of partially coherent beam, Opt. Commun. **281**, 1968 (2008).

[37] I. Takeda, T. Yoda, Y. Moritake, K. Takata, and M. Notomi, "Dataset for propagation and circulating modes of reciprocal non-Hermitian skin effect (2025)", figshare, https://doi.org/10.6084/m9.figshare.30295099.v1.